

CHARMM Force Field for Protonated Polyethyleneimine

Titus Adrian Beu, * Andrada-Elena Ailenei, and Alexandra Farcaș

We present a revised version of our previously published atomistic Chemistry at Harvard Macromolecular Mechanics (CHARMM) force field for polyethyleneimine (PEI). It is based on new residue types (with symmetric $-C-N-C-$ backbone), whose integer charges and bonded parameters are derived from ab initio calculations on an enlarged set of model polymers. The force field is validated by extensive molecular dynamics simulations on solvated PEI chains of various lengths and protonation patterns. The profiles of the gyration radius, end-to-end distance, and diffusion coefficient fine-tune our previous

results, while the simulated diffusion coefficients excellently reproduce experimental findings. The developed CHARMM force field is suitable for realistic atomistic simulations of size/protonation-dependent behavior of PEI chains, either individually or composing polyplexes, but also provides reliable all-atom distributions for deriving coarse-grained force fields for PEI. © 2018 Wiley Periodicals, Inc.

DOI:10.1002/jcc.25637

Introduction

The design and practical development of effective gene carriers, featuring high transfection efficiency, specificity, and biocompatibility, are central to many modern gene delivery protocols.^[1–5] Widely used as a nonviral gene vector, polyethyleneimine (PEI: $-[CH_2-CH_2-NH]_n-$) occurs in linear or branched configurations. If protonated (with the NH groups partially replaced by NH_2^+ groups), PEI shows a considerable buffering capacity which enables the condensation of DNA into polyplexes via electrostatic interactions between the protonated units and the negative phosphate groups of DNA.

Due to inherent difficulties associated with developing realistic atomistic or coarse-grained force fields (FFs) for polycations, the number of theoretical/computational papers dealing in detail with solvated PEI chains or DNA-PEI polyplexes is rather limited. Even though some updates of the CHARMM FF significantly improved the treatment of DNA,^[6,7] in order to conclusively investigate DNA-PEI condensation, a reliable FF for PEI is still needed. In one of the first systematic computational studies on the formation of DNA-polycation complexes, Ziebarth et al.^[8] employed the Amber gaff FF^[9] (notably not specifically parametrized for PEI) and, acknowledging the charge distribution around the DNA helix to be the key issue to understanding DNA condensation, optimized the partial charges by the restrained electrostatic potential (RESP) method^[10] based on ab initio data. The same atomistic FF was used in subsequent investigations on the protonation behavior of solvated linear PEI^[11] and also in a recent study on PEI-DNA and PEI-siRNA complexes.^[12] The molecular dynamics (MD) studies of Choudhury et al.^[13] on the solvation dynamics of linear PEI essentially employed the same Amber FF, without notable improvements. Equally starting from the Amber FF, the partial charges of PEI were derived in the studies of Kondinskaia et al.^[14] from ab initio calculations on four model trimers by the RESP method.

The MD simulations on solvated DNA-PEI complexes of Sun et al.^[15] adopted residues by analogy from the CHARMM27 FF,^[16] and the torsional parameters, identified to be important, were improved by fits to ab initio data. As a first step in developing a coarse-grained MARTINI FF for modeling the complexation of RNA, Wei et al.^[17] developed an atomistic FF for polyethylene-glycol-grafted linear PEI based on the CHARMM General Force Field (CGenFF)^[18] using a “divide-and-conquer” strategy applied to small polymer building blocks. The dihedral parameters, in particular, were optimized relative to ab initio potential energy scans by using the Force Field Toolkit (ffTK).^[19]

Aiming for a more realistic modeling of the size- and protonation-dependent behavior of PEI, we recently published a new CHARMM FF for linear PEI.^[20] As a major difference with respect to previous parametrizations, along with the partial atomic charges, we consistently adjusted the *whole* set of bonded parameters (for bonds, angles, and dihedrals), not only the dihedral contributions. The quality of the parametrization was enhanced by a more comprehensive body of basic ab initio data used in the optimization procedure (carried out by means of the ffTK application), namely stemming from two PEI model tetramers. Defining residues with $-C-C-N-$ backbone, we actually implemented a generic nonprotonated residue type and *two* fractionally charged residue types, the latter being employed in pairs to model the unitary protonation charge, which, according to the ab initio charge distributions, extends beyond the limits of single PEI monomers. Another

T. Adrian Beu, A. Ailenei, A. Farcaș
University Babeș-Bolyai, Faculty of Physics, Department of Biomolecular Physics,
1 Mihail Kogălniceanu Street, Cluj-Napoca 400084, Romania
E-mail: titus.beu@phys.ubbcluj.ro

Contract Grant sponsor: Executive Unit for Financing Higher Education, Research, Development and Innovation (UEFISCDI); Contract Grant number: PN-III-P4-ID-PCE-2016-0474

© 2018 Wiley Periodicals, Inc.

notable aspect of our published FF compared to earlier studies was the increased stiffness of the modeled PEI chains.

This article introduces a revised version of our previous CHARMM FF for PEI, emerging from a slight shift of perspective and a more nuanced balance of the various modeling options. With a view to further develop a coarse-grained version of the FF, we chose to implement only residue types with *symmetric* backbone $-C-N-C-$. The price paid for the assumed residue symmetry was the constraint to confine the rather extended unitary charge distribution about protonated sites to a single residue type. Nevertheless, we essentially achieved a fine-tuning of our initial CHARMM FF for PEI by defining a smaller number of symmetric residue types and using an enlarged set of (three) model pentamers to produce the reference ab initio data used in the optimization procedure. After describing the basic modeling, optimization, and simulation aspects, we present in detail the FF parametrization procedure and MD simulation results for solvated PEI chains of various sizes and protonation patterns. At each step, we analyze the present results in relation to those from our previous paper.^[20]

The present article actually opens a sequence of follow-up papers. Based on the atomistic data reported here, the next paper presents a coarse-grained (MARTINI) version of our atomistic FF for PEI and associated MD simulations. Further on, we will develop our atomistic and coarse-grained FFs for branched and grafted PEI.

Methodology

Adjustment of the CHARMM force field

CHARMM^[16,18,21] is one of the most versatile and commonly used atomistic FF models, being implemented in many state-of-the-art MD simulation packages. The CHARMM model is additive and explicitly accounts for bonded and nonbonded interactions:

$$U_{\text{bonded}} = \sum_{\text{bonds}} k_b(b-b_0)^2 + \sum_{\text{angles}} k_\theta(\theta-\theta_0)^2 + \sum_{\text{dihedrals}} k_\psi[1 + \cos(n\psi - \delta)] + \sum_{\text{impropers}} k_\omega(\omega-\omega_0)^2 + \sum_{\text{Urey-Bradley}} k_{\text{UB}}(b^{1,3}-b_0^{1,3})^2 \quad (1)$$

$$U_{\text{nonbonded}} = \sum_{\text{atoms } i,j} \left\{ \frac{q_i q_j}{\epsilon_0 r_{ij}} + \epsilon_{ij} \left[\left(\frac{r_{ij}^{\text{min}}}{r_{ij}} \right)^{12} - 2 \left(\frac{r_{ij}^{\text{min}}}{r_{ij}} \right)^6 \right] \right\}, \quad (2)$$

where

$$r_{ij}^{\text{min}} = (r_i^{\text{min}} + r_j^{\text{min}})/2, \epsilon_{ij} = \sqrt{\epsilon_i \epsilon_j}. \quad (3)$$

The bonded potential terms comprise bond-stretching, angle-bending, dihedral, improper dihedral, and Urey-Bradley contributions, whereby k_b , k_θ , k_ψ , k_ω , and k_{UB} are the respective force constants. In addition, b_0 and θ_0 are equilibrium bond lengths and angles, respectively, and the dihedrals are

characterized by multiplicities n and phases δ . For the particular purpose of modeling PEI, improper angles and Urey-Bradley terms are not relevant. The nonbonded electrostatic and van der Waals interactions are characterized by the atomic charges q_i and, respectively, the potential well depths ϵ_{ij} and Lennard-Jones radii r^{min} .

As in our previous work,^[20] in (re)parametrizing the CHARMM FF for PEI, we followed the methodology implemented in the fTK v1.1 tool kit,^[19,22] employed as a plugin of the visualization/analysis application VMD.^[23] In essence, we optimized the atomic charges, along with the force constants and equilibrium values for bonds, angles, and dihedrals, relative to quantum mechanical (QM) data generated using Gaussian 09 Rev. A.01.^[24] While, in general, the calculations were done at MP2/6-31G(d) level, to maintain consistency with the standard CHARMM FF, we used the HF/6-31G(d) level for determining the atomic charges from interactions with water. The complex multistage optimization procedure actually involved performing the steps outlined below for the three PEI model pentamers defined in the section.

1. The Lennard-Jones parameters were assigned to each atom type of PEI by analogy with atom types defined in the CHARMM36 CGenFF.^[25]
2. The partial atomic charges of PEI were adjusted with respect to QM PEI-water interaction profiles and dipole moments compiled from separate PEI-(single-H₂O-molecule) optimizations.
3. The bond and angle parameters were optimized by fitting total QM and molecular mechanics (MM) equilibrium bond and angle values, along with their distortion energies calculated from Hessian matrices in internal coordinates (ICs).
4. The dihedral parameters were adjusted based on explicit QM torsion scans for the dihedrals of interest, by minimizing the difference between the QM and MM torsion energy surfaces.

Molecular dynamics

All the reported atomistic MD simulations were performed with the NAMD v2.12 code^[26] using a 2 fs time step and the SHAKE algorithm^[27] to keep the bonds involving H atoms fixed. For the short-range nonbonded interactions, we applied a smoothing function with a switch distance of 10 Å and a cutoff of 12 Å. We used cubic simulation boxes with periodic boundary conditions and the CHARMM TIP3P water model^[28] to solvate the studied PEI polymers.

The long-range electrostatics under periodic boundary conditions was treated by means of the particle mesh Ewald (PME) method,^[29] using a 1 Å mesh spacing. Without a notable loss of accuracy, the k -space contributions were updated at every second step. We employed a Langevin thermostat with a damping coefficient of 1 ps⁻¹ to keep the temperature fixed at 310 K, and a Langevin piston^[30,31] with a decay constant of 50 fs to fix the pressure at 1 atm.

Results and Discussion

Parametrization of the CHARMM FF

Definition of residues. The reparametrized version of our CHARMM FF for PEI chains presented here reflects, as already pointed out, a slight change of focus regarding the intended use of the FF. The underlying ideas are:

1. Define *as few* residue and atom types as necessary for building solvated PEI chains of arbitrary lengths and protonation patterns with realistic dynamic/structural behavior.
2. Identify residues with entire *functional groups*.
3. Define residues with *integer charge* (0 or 1) to comply with the CHARMM standard.
4. Define residues with *symmetric backbone* ($-C-N-C-$), so as to be mappable to single coarse-graining (CG) beads in a follow-up residue-based CG parametrization.

Guided by these ideas, we defined three residue types: PEI—generic unprotonated $CH_2-NH-CH_2$ monomer; PEP—protonated $CH_2-NH_2^+-CH_2$ monomer; and PEC—terminal CH_3 (methyl) group starting and ending each PEI chain.

To derive the FF parameters from QM calculations, we considered three linear PEI model pentamers (Fig. 1), chosen to display the essential features of protonated/unprotonated PEI chains: PEI5p0—nonprotonated (PEC-PEI-PEI-PEI-PEI-PEC); PEI5p1—singly protonated at the central residue (PEC-PEI-PEI-PEP-PEI-PEC); and PEI5u2—uniformly protonated at every second residue (PEC-PEI-PEP-PEI-PEP-PEI-PEC). The three model pentamers are respectively composed of 48, 49, and 50 atoms. Compared to the just two model tetramers used in our previous study (PEI4p0 and PEI4p1),^[20] we were able to extract more reliable MM data from the three central monomers, which are

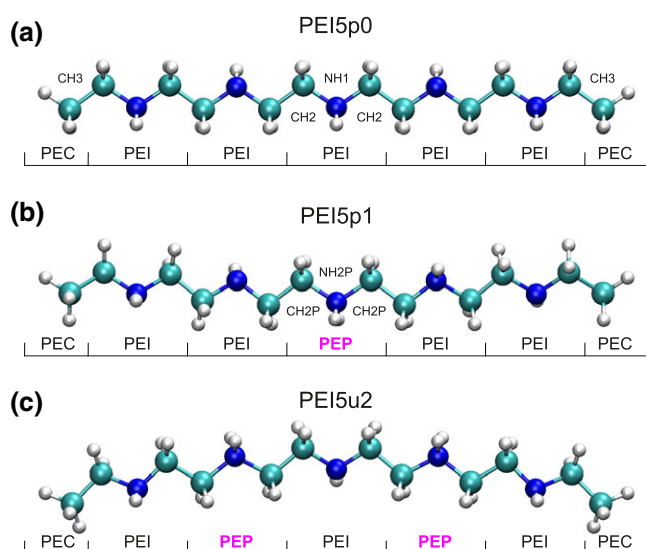


Figure 1. PEI model pentamers used in the parametrization of the CHARMM force field (a) unprotonated, (b) protonated at the central nitrogen, and (c) uniformly [alternatively] protonated, showing the composing residues and atom types. [Color figure can be viewed at wileyonlinelibrary.com]

obviously less perturbed by the terminal methyl groups. Also, PEI5u2 is the shortest PEI model that can accommodate uniform 1/2-protonation, providing information on angles and dihedrals involving alternations of protonated/nonprotonated units.

To account for the relevant vicinities of the backbone atoms, we defined nine atom types as follows: NH1—N atom of NH group (within the PEI residue); HNH1—H atom bonded to NH1; NH2P—N atom of protonated NH_2^+ group (within the PEP residue); HN2P—H atom bonded to NH2P; CH2—C atom bonded to NH1 (within the PEI residue); CH2P—C atom bonded to NH2P (within the PEP residue); HC2—H atom bonded to CH2 or CH2P; CH3—C atom of terminal CH_3 group (within the PEC residue); and HC3—H atom bonded to CH3.

As compared to our previous model, we reduced by two the number of residue types and by one the number of atom types. In addition, all residue types are symmetric and carry an integer charge. It should be noted, however, that these simplifications have been possible at the expense of more significant final corrections needed in the partial atomic charges to restrain the entire protonation charge to a single residue type (PEP). In our previous model, two residue types, denoted as PEP and PEQ, carrying fractional charges, were defined to jointly model the unitary charge and the spatially rather extended charge distribution about the central NH_2^+ group, while the smooth transition of parameter values between the protonated (NH2P) and nonprotonated (NH1) sites was ensured by an additional carbon atom type (CH2X), which is no longer present.

With the model polymers, residues, and atom types defined as explained, we carried out a rigorous optimization of the partial atomic charges in conjunction with the bond, angle, and dihedral parameters according to the work flow set out by Vanommeslaeghe et al.^[18] and implemented within fTK.

Since, for any given atom type, the MM parameters yielded by the fTK optimization procedures inherently show variations depending on the location within the polymer, both for the PEI and PEP residue types we chose to consistently consider the average parameters over the *three central residues* of all three model pentamers, which are less perturbed by the polymer ends. As for the atom types of the terminal PEC residue, we considered averages over all occurrences within the model pentamers.

Our present PEI residue types are similar to those of Wei et al.,^[17] for which, however, standard (nonspecific) values were adopted for charges, as well as for bond and angle parameters, while only the dihedral contributions were optimized based on QM data extracted from model trimers (obviously more sensitive to terminal groups than the pentamers).

Lennard-Jones parameters by similarity. According to the general methodology implemented in fTK, we assigned the Lennard-Jones parameters to each atom type by analogy, from similar atom types defined in the CHARMM CGenFF FF,^[25] as listed in Table S1 of Supporting Information. Except for the atom types associated with the methyl group, these parameters are also the ones used in our previous work.^[20]

Partial atomic charges from PEI–water interaction profiles.

Critically reevaluating our previous PEI model,^[20] its increased number of residue and atom types compared to other available models is obviously a consequence of the asymmetric definition of the residues. While this very aspect enabled a more nuanced modeling of the charge distributions about protonated sites, which extend (according to the QM calculations) beyond the boundaries of single residues, it also involved, as indicated above, defining two protonated residue types—one for starting and another for ending protonated segments—with different fractional charges and jointly yielding unitary charge. Conversely, we explored in the present work the (somewhat more artificial) alternative of restraining the supplementary unitary protonation charge to a single symmetric residue type, and minimizing the entailed inaccuracies by enlarging the set of model polymers from which the QM target data were extracted. Obviously, the so defined residue type is suitable for modeling single protonated sites separated by non-protonated segments, however not for continuously protonated segments, and even less for transitions between these and unprotonated segments. In fact, we were interested in uniform protonation patterns, not denser than alternative protonation (at every second PEI monomer).

Following the CHARMM conventions and the methodology implemented in fTK,^[19] to realistically model solvated systems, the water-accessible atoms of the PEI model pentamers were identified as hydrogen bond donors (H atoms) or acceptors (N atoms of unprotonated NH groups). For each target atom, a PEI-(single-H₂O-molecule) complex was built, optimizing quantum mechanically (at HF/6-31G(d) level, for consistency with the CHARMM standard) the distance and rotation angle of the H₂O molecule, with all other degrees of freedom fixed. Also, in accordance with the standard CGenFF operation, to better approximate the bulk phase for neutral compounds solvated in TIP3P water, the QM-optimized distances for PEI5p0 were reduced by 0.2 Å and the interaction energies were scaled by a factor of 1.16. By contrast, no corrections were applied to the protonated models PEI5p1 and PEI5u2. The QM sets of distances, interaction energies, and dipole moments were then jointly used as target data in repeated optimizations of the atomic charges, imposing, in addition, neutrality for PEI5p0, unitary net charge for PEI5p1, and a +2e net charge for PEI5u2. In particular, all aliphatic H atoms were assigned the standard charge +0.09e and were excluded from the optimization. To

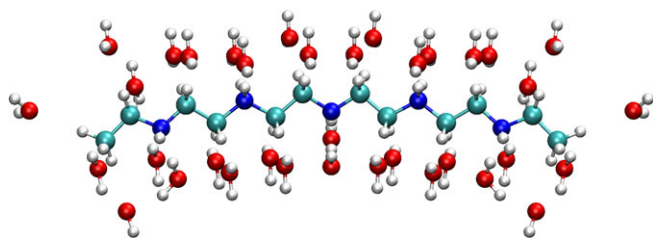


Figure 2. Superimposed optimized configurations of complexes formed by the alternatively protonated pentamer PEI5u2 with test water molecules, used for adjusting the atomic charges. [Color figure can be viewed at wileyonlinelibrary.com]

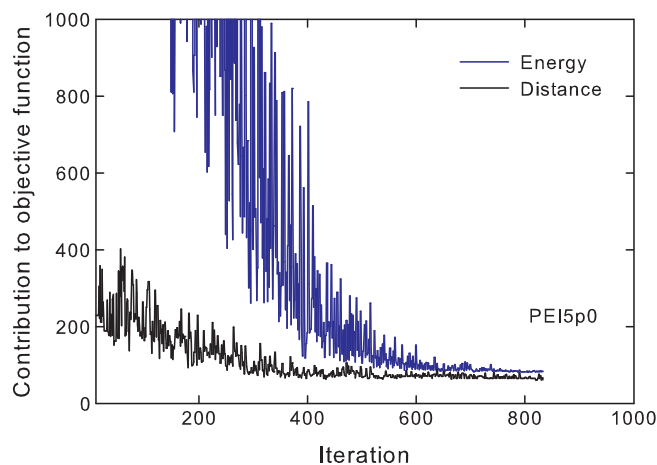


Figure 3. Reduction of the distance and energy contributions to the objective function during the optimization process of the partial atomic charges for the unprotonated pentamer PEI5p0. [Color figure can be viewed at wileyonlinelibrary.com]

illustrate the procedure, the superimposed configurations of all the optimized PEI5u2-H₂O complexes are depicted in Figure 2.

Figure 3 illustrates the rapid convergence of the distance and energy contributions to the objective function during the optimization procedure of the partial atomic charges for the unprotonated pentamer model. The contributions of the dipole moment to the objective function can be seen in Figure S1 of Supporting Information to exhibit a similarly fast convergence.

Table S2 of Supporting Information lists the partial charges yielded by the fTK optimization for all occurrences of each atom type composing the PEI residue, as part of the three central monomers (no. 2, 3, and 4) of all the three model pentamers. Similarly, Supporting Information Table S3 shows the atomic charges for the atom types composing the PEP residue within the protonated models PEI5p1 and PEI5u2. The averages over all occurrences of each atom type, as part of either PEI or PEP, are collected as $\langle Q_{\text{fTK}} \rangle$. Sticking to the rule of aliphatic hydrogens (HC2 and HC3) being attributed the standard charge +0.09e and imposing neutrality on the terminal PEC residue, the CH3 atom type was simply assigned the charge $-0.27e$, and thus the terminal atom types were actually excluded from the optimization.

As the average net charges of the residues PEI (0.023e) and PEP (0.894e) do not amount to integer values, as required by the CHARMM standard, further adjustments are necessary. We choose to distribute the total complementary correction charges ΔQ ($-0.023e$ and $0.106e$, respectively) equally among all but aliphatic H atoms, resulting in small atomic corrections which do not exceed $0.006e$ for PEI and $0.022e$ for PEP. This approach leads to the final partial atomic charges listed as Q_{final} , which ensure neutrality for PEI and unitary charge for PEP.

Due to the identical atomic composition of our present and former PEI residue types, a direct comparison of the optimized charges is possible (see Table 1). While for the NH group, the “old” charges (Q_{old}) can be seen to differ rather little (by not more than 4%) from the present values (Q_{final}), in the case of

Table 1. Average atomic charges for the PEI residue ($\langle Q_{\text{ffTK}} \rangle$) (in units of e) resulted from the ffTK optimization procedure of the three model pentamers (see also Supplementary Information). Q_{final} are the final optimized partial charges, rescaled to ensure neutrality, whereby $\Delta Q = Q_{\text{final}} - \langle Q_{\text{ffTK}} \rangle$ are the applied corrections. For comparison, the values Q_{old} of our previous parametrization^[20] are also given, along with the corresponding relative differences δQ_{old} .

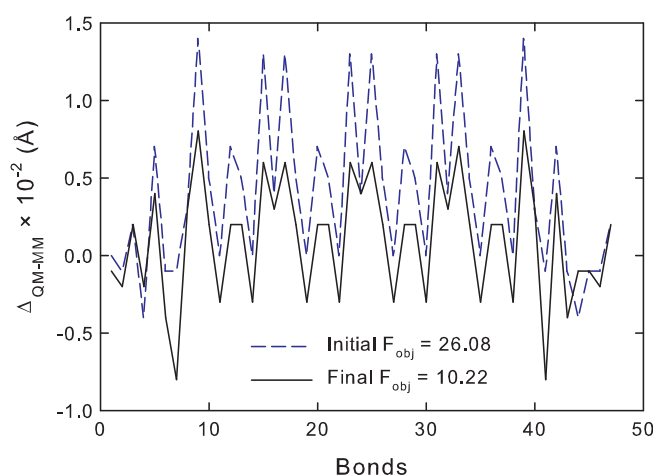
Residue	Atom types	No. of atoms	$\langle Q_{\text{ffTK}} \rangle$ e	Q_{final} e	ΔQ e	Q_{old} e	δQ_{old} %
PEI	CH2	2	0.040	0.034	-0.006	0.044	22.7
	HC2	4	0.090	0.090	0.000	0.090	0.0
	NH1	1	-0.758	-0.764	-0.006	-0.796	4.0
	HNH1	1	0.341	0.336	-0.005	0.348	3.4
	q_{tot}	8	0.023	0.000	-0.023	0.000	

the CH₂ group the relative differences δQ_{old} rise as high as 23%. The significantly larger differences in the latter case are a direct consequence of the fact that the present CH₂ atom type cumulates the functionalities of both the former CH₂ and CH_{2X} types, with CH_{2X} conceived to ensure a more gradual transition between the PEI and PEP residues.

Bond and angle parameters from distortion energies.

The iterative approach implemented in ffTK for optimizing bond stretching and angle bending parameters essentially matches the total QM and MM distortion energies, defined to cumulate all the contributions from the Hessian matrix in the representation of ICs (i.e., bonds, angles, and so forth). Indeed, as the Hessian matrix characterizes the local curvature of the potential energy surface, it can be used within the harmonic approximation to describe finite energy variations caused by small distortions of the ICs about the equilibrium configuration. QM Hessian matrices are readily obtained in vibrational calculations with Gaussian and are used for calculations of energies for bond and angle distortions in ffTK. The corresponding MM energies for the distortions are calculated from the applied FF parameters.

For the unprotonated model pentamer, the deviations of the MM equilibrium bond lengths from the QM reference values are illustrated in Figure 4. Although they are rather small

**Figure 4.** Differences between the MM and QM equilibrium bond lengths for PEI5p0 in the initial and final optimization steps, along with the corresponding objective function values F_{obj} . [Color figure can be viewed at wileyonlinelibrary.com]

already after the initial optimization step, they drop under 10^{-2} Å (in absolute value) after the final iteration, with balanced negative and positive contributions, indicating a very good agreement between the QM and MM values, and the objective function (jointly accounting for the QM-MM geometry and energy differences) decreasing significantly. For the equilibrium angles, a similar reduction of the QM-MM differences can be seen in Figure S2 of Supporting Information.

The equilibrium bond lengths and force constants obtained for each of the three model pentamers by applying the ffTK optimization procedure are compiled in Table S4 of Supporting Information, along with the final parameter values, defined as averages over all models. The final parameters for the backbone atoms are listed in Table 2, where they are compared with the corresponding values of our previous model. As it can be noted, the deviations in the force constants do not exceed 3.3%, while the equilibrium bond lengths differ by not more than 0.5%.

As previously, protonation does not significantly affect the length of the C–C bond. However, CH₂ atoms can be seen to bind more strongly (by roughly 12%) to NH₁ ($335.7 \text{ kcal mol}^{-1} \text{ \AA}^{-2}$) than to CH₂ atoms ($299.0 \text{ kcal mol}^{-1} \text{ \AA}^{-2}$), which supports a symmetric definition of the PEI residue (with CH₂–NH₁–CH₂ backbone). We note that the protonated bond NH_{2P}–CH_{2P} is notably weaker than the unprotonated one, NH₁–CH₂, a slight increase in the equilibrium length (1.488 Å vs. 1.453 Å) being accompanied by a 20% lower force constant.

The optimized angular parameters provided by the ffTK procedure for each of the model pentamers are collected in Table S5 (Supporting Information), together with the final values, which are the averages over all models. For the backbone atoms, the final angular parameters are summarized in Table 3, along with their counterparts from our previous model. Comparing our two FF parametrizations it can be noted that, while the nonprotonated angles (CH₂–CH₂–NH₁ and CH₂–NH₁–CH₂) practically conserve their equilibrium values and differ in terms of force constants by less than 5%, the force constants for the protonated angles between protonated and unprotonated monomers (CH₂–CH_{2P}–NH_{2P} and CH_{2P}–CH₂–NH₁) show large relative differences, exceeding 29% in the case of CH_{2P}–CH₂–NH₁. The cause for the discrepancies is again linked to the absence of the CH_{2X} transition atom type in our present parametrization.

As a general finding, protonation renders the angles stiffer, both inside and between the residues. In particular, the force constant for the CH₂–CH_{2P}–NH_{2P} angle exceeds by almost

Table 2. Optimized force constants k_b and equilibrium bond lengths b_0 for the backbone atom types, along with the absolute relative differences, δk_b and δb_0 , with respect to the bond stretching parameters k_b^{old} and b_0^{old} of our previous model.^[20]

Atom		k_b	b_0	k_b^{old}	b_0^{old}	δk_b	δb_0
types		(kcal mol ⁻¹ Å ⁻²)	(Å)	(kcal mol ⁻¹ Å ⁻²)	(Å)	(%)	(%)
CH2	CH2	299.0	1.515	289.0	1.514	3.3	0.1
CH2	CH2P	280.8	1.511	288.4	1.512	2.7	0.1
CH2	NH1	335.7	1.453	332.4	1.446	1.0	0.5
CH2P	NH2P	268.4	1.488	276.5	1.496	3.0	0.5
CH3	CH2	312.1	1.525				

13% the one for CH2—CH2—NH1. Similarly, for the CH2P—NH2P—CH2P angle, the force constant is 9% larger than for CH2—NH1—CH2 (quite in contrast to the CH2P—NH2P bond, which, as shown above, is weaker than CH2—NH1). As expected, the equilibrium length of fully extended PEI polymers increases with the protonation fraction (see Supporting Information Table S7), and this is both due to the larger CH2P—NH2P—CH2P angle and slightly longer CH2P—NH2P bond.

As the sequence PEP-PEQ-PEP needed for modeling alternate protonation comprises in the present model via the PEI5u2 pentamer, no parameters needed to be adopted by similarity like in our previous approach, thereby a former weakness being eliminated.

Dihedral parameters from torsion scans. The Hessian-matrix approach, which proves to be the method of choice for bond and angle optimizations, is not actually useful for dihedral angles. Indeed, even though the Hessian appropriately models the local energy surfaces of the ICs about the minimum, for dihedral angles the FF must accurately treat also the high energy regions, where the harmonic approximation is not applicable. Specifically, the procedure implemented in fTK uses scans of torsion coordinates to adjust periodic potential wells characterized by force constants k_{θ} , multiplicities n , and phases δ [see eq. 1]. As per convention, the phases are fixed at either 0° or 180°, while the multiplicities are assigned nonzero integer values based on local symmetry considerations.

According to the general methodology, we restricted the QM scans to dihedrals involving only backbone atoms, including all the dihedrals in the subsequent optimization procedure. Each QM scan implied a sequence of MP2/6-31G(d) geometry optimizations for fixed distortions of the targeted dihedral angle, covering the symmetric range between -90° and +90° in steps of 10° and allowing the rest of the molecule to relax freely. The differences between the QM and MM potential energy surfaces

for the entire set of scanned dihedrals were minimized iteratively, in hundreds of simulated annealing/downhill processes for each PEI model pentamer.

We first adjusted the dihedral parameters for the unprotonated model PEI5p0. Thereupon, adopting the multiplicities and shifts (n and δ) for the dihedrals shared with PEI5u2, we adjusted all the force constants for the latter, along with the multiplicities and shifts for the disjoint dihedrals (involving protonated atomic species). Finally, adopting the adjusted values n and δ from PEI5p0 and PEI5u2, we optimized all the dihedral force constants for the singly protonated model PEI5p1, thereby ensuring consistency of the multiplicities and shifts for all occurrences of each given dihedral angle across all pentamer models.

For selected dihedrals, the QM energy scans are plotted along with the fitted MM torsion profiles in Figure 5 for PEI5p0 and in Figure 6 for PEI5p1 and PEI5u2. The optimized dihedral parameters resulted for each of the pentamer models are listed in Table S6 (Supporting Information), which also includes as final force constants the averages over the individual model pentamers. The final multiplicities and shifts obviously coincide with those of the individual sets.

Figures 5 and 6 evidence a very good agreement between the MM torsion profiles and the corresponding QM references. In fact, the overall root-mean-square error (RMSE) achieved for PEI5p0 (0.10) is significantly lower than the value reported by Wei et al.^[17] for a PEI1p0 model (0.59), being even lower than for our previous unprotonated model PEI4p0 (0.17). Also, comparing our previous protonated model PEI4p1 with PEI5p1, the RMSE drops from 0.25 to 0.19. The superior quality of our present torsional contributions is clearly a consequence of the fact that we consistently adjusted the *entire* set of bonded parameters based on an *enhanced* set of (longer) PEI models, with more representative protonation patterns. The larger RMSEs for PEI5u2 (0.31) and PEI5p1 (0.19)

Table 3. Optimized force constants k_{θ} and equilibrium angles θ_0 for the backbone atom types, along with the absolute relative differences, δk_{θ} and $\delta \theta_0$, with respect to the angle bending parameters k_{θ}^{old} and θ_0^{old} of our previous model.^[20]

Atom			k_{θ}	θ_0	k_{θ}^{old}	θ_0^{old}	δk_{θ}	$\delta \theta_0$
types			kcal mol ⁻¹ rad ⁻²	deg	kcal mol ⁻¹ rad ⁻²	deg	%	%
CH2	CH2	NH1	62.6	109.8	64.9	109.7	3.6	0.0
CH2	CH2P	NH2P	71.1	109.7	80.3	111.5	13.0	1.6
CH2	NH1	CH2	70.3	110.8	67.1	110.9	4.5	0.1
CH2P	CH2	NH1	69.8	107.0	90.4	106.4	29.4	0.5
CH2P	NH2P	CH2P	76.8	113.5	73.6	114.2	4.1	0.6
CH3	CH2	NH1	97.2	112.6				

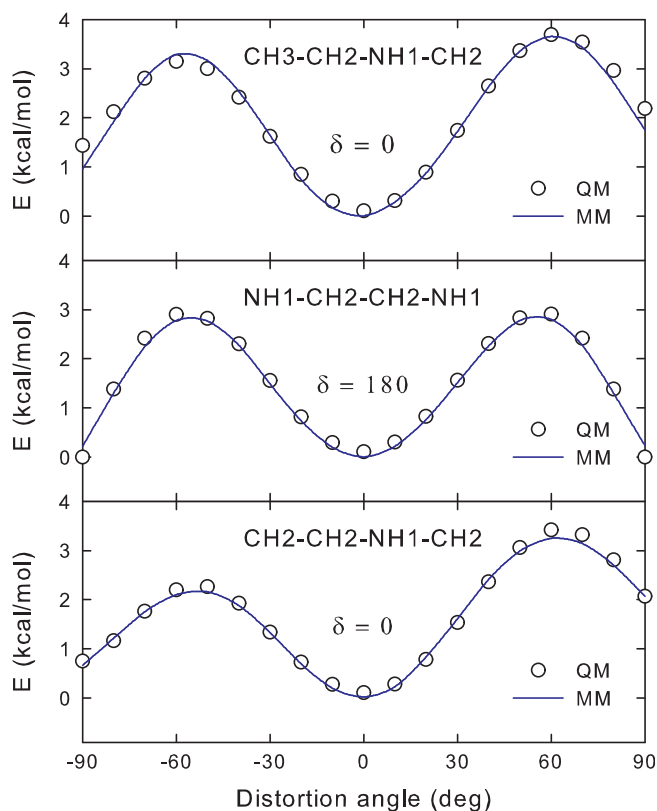


Figure 5. Torsion energy profiles for dihedrals defining the backbone of the unprotonated model pentamer PEI5p0. [Color figure can be viewed at wileyonlinelibrary.com]

than for PEI5p0 can be traced back to the larger corrections needed to confine the unitary protonation charge to a single residue type (PEP), than the ones required to make the generic PEI residue neutral.

Protonation appears to weaken the backbone dihedral N–C–C–N, contrary to the angle CH2–CH2P–NH2P being stiffer than CH2–CH2–NH1. In fact, the force constants for NH1–CH2–CH2–NH1 and NH1–CH2–CH2P–NH2P differ by an order of magnitude (2.734 kcal mol⁻¹ vs. 0.285 kcal mol⁻¹).

Being affected by the whole sequence of preceding optimizations (of charges, bonds, and angles), and only expected to achieve a fine-tuning of the FF, our present and former dihedral parameters are rather difficult to compare. Nevertheless, the most rigid dihedral remains NH1–CH2–CH2–NH1 (old force constant 2.999 kcal mol⁻¹). Also, in the presence of protonation, we note a transfer of dihedral rigidity to CH2P–NH2P as central bond, with a more than double force constant for CH2–CH2P–NH2P–CH2P (0.732 kcal mol⁻¹) as compared to the old value (0.3260 kcal mol⁻¹).^[20]

Overall, both our old and present FF parametrizations model more rigid PEI polymers than in the literature. For example, the dihedral force constants reported by Sun et al.^[15] amount to only 0.15 kcal mol⁻¹ for NH1–CH2–CH2–NH1 and 0.10 kcal mol⁻¹ for CH2–CH2P–NH2P–CH2P (roughly 5% and 14%, respectively, of our values). The remarkable differences are clearly a direct consequence of the fact that we used pentamers as model compounds, instead of monomers, in the cited work. In addition, we

consistently optimized the *full* set of bonded parameters and atomic charges, not solely the dihedrals.

The complete set of parameters adjusted according to the procedure described in this section is provided as Supporting Information.

MD simulations of solvated PEI chains

We employed our new CHARMM parametrization in systematic MD simulations of solvated linear PEI chains, similar to those reported in our previous paper.^[20] To enable a conclusive analysis of the dynamic structuring both in terms of length and protonation, throughout we considered uniform protonation fractions equal to 0 (unprotonated), 1/4 (one-in-four), 1/3 (one-in-three), and 1/2 (alternative). PEI chains that are able to accommodate such uniform protonation patterns and have unprotonated first and last monomers (adjoining the ending CH₃ units) are composed of 12*n* + 3 monomers. Concretely, we considered for each of the aforementioned protonation fractions PEI 27-mers, 39-mers, and 51-mers, up to a total of 12 size (protonation fraction) combinations. Alternative protonation, in particular, is relevant both in experiments and for comparisons with the literature.

A summary of the main features of the simulated systems is given in Table S7 (Supporting Information). The listed chain lengths actually cumulate the equilibrium lengths of the composing residues, as resulting from the QM optimizations of the model pentamers. They appear to slightly increase with the protonation fraction, which can be certainly related to the buildup

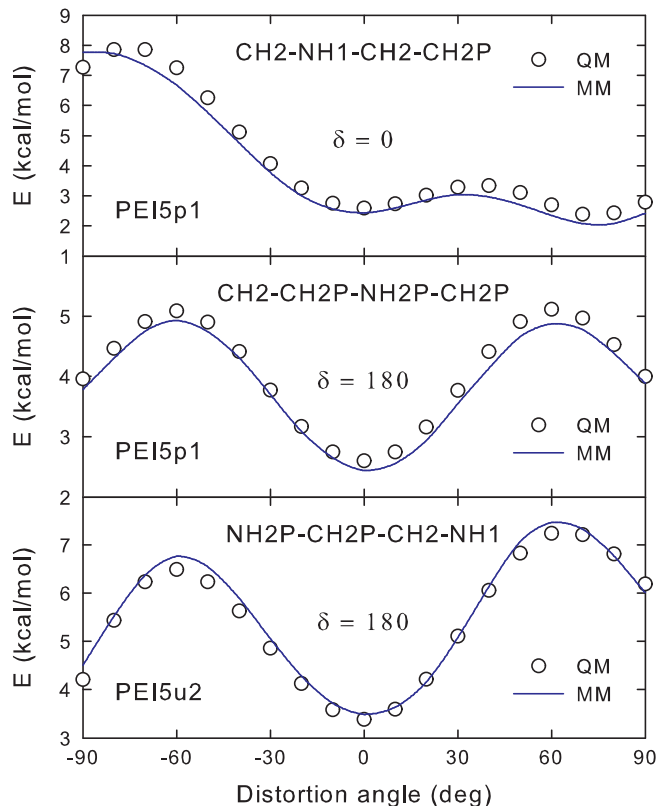


Figure 6. Torsion energy profiles for dihedrals involving protonated backbone species of the model pentamers PEI5p1 and PEI5u2. [Color figure can be viewed at wileyonlinelibrary.com]

of electrostatic repulsion. The neutrality of all the solvated systems simulated was ensured by adding a number of Cl^- counterions matching the number of protonated PEI monomers.

The initial size of the simulation box was set large enough to screen the chain's interactions with its periodic replicas. More precisely, the simulation box for PEI27 was able to spaciouly accommodate the fully stretched polymer on the diagonal. For PEI39 and PEI51, we no longer could increase the box in a similar proportion; nevertheless, its size exceeded by at least 50% the final average gyration radius of the polymer.

For each of the 12 size-(protonation fraction) combinations, we achieved a total of 400 ns of data collection, cumulated from sets of 20 trajectories of 21 ns each. Technically, the last configuration of each trajectory was used as the initial configuration for the next one, however, discarding the first nanosecond in order to reduce time correlations and improve statistics. In particular, to produce the initial configuration for the first trajectory, we equilibrated a solvated helical PEI chain for 3 ns. Figure 7 shows a snapshot from a typical trajectory for the alternatively protonated PEI 51-mer.

Gyration radius, end-to-end distance, and persistence length. To measure the spatial extent of the simulated PEI chains, we employed the commonly used gyration radius, R_g , and end-to-end distance, D_{ee} (the latter defined by the N atoms of the first and last PEI monomer). The time evolution profiles of the ensemble-averaged R_g and D_{ee} for the unprotonated 27-mer and for all protonation patterns of the 51-mer are comparatively depicted in Figure 8 (throughout the article, black stands for unprotonated chains, and blue, green, and red for 1/4, 1/3, and 1/2 protonation, respectively). As expected, the average levels for these quantities show a pronounced increase both with the chain length and protonation

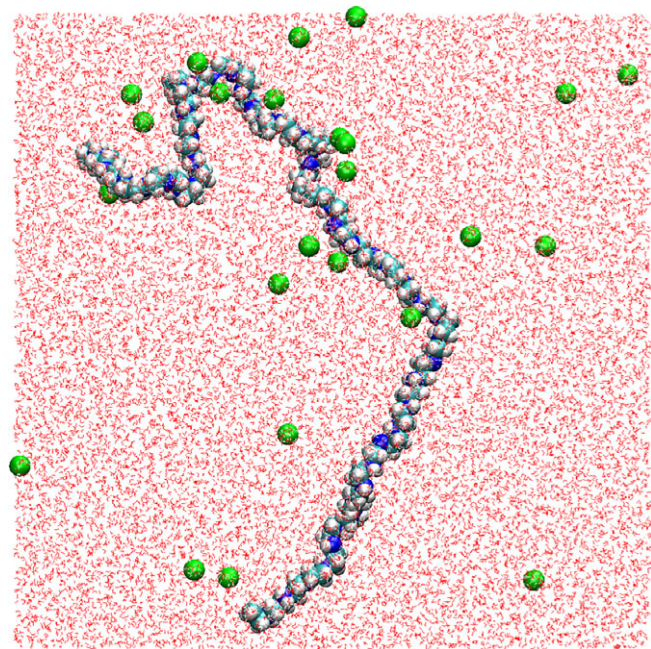


Figure 7. Snapshot from a trajectory of the alternatively protonated PEI 51-mer (PEI51u2). [Color figure can be viewed at wileyonlinelibrary.com]

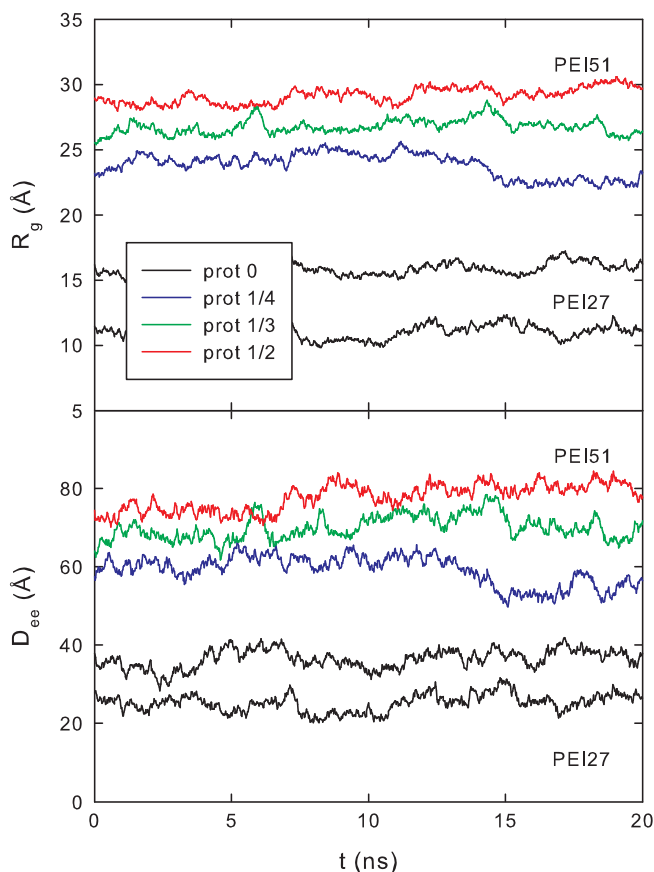


Figure 8. Time evolution of ensemble-averaged gyration radius and end-to-end distance for solvated PEI 27-mers and 51-mers. To avoid curve congestion, for the 27-mers only the (lowest) profiles for the nonprotonated PEI27p0 are plotted. [Color figure can be viewed at wileyonlinelibrary.com]

fraction. A similar increase of D_{ee} (derived from NMR spectrometry measurements of translational diffusion coefficients) with the chain size was reported by Schubert et al.^[32] for PEI chains with molecular weights in the range 1100 to 13,900 g mol^{-1} .

To give a sense of the spread of spatial extents over the entire 400 ns of data collection, Figure 9 depicts the probability distribution of the time- and ensemble-averaged gyration radius for the 1/3-protonated 51-mer. The graph also includes snapshots of conformations that are representative for the high-probability region (around 27 Å) and, respectively, for the low-probability sides of the distribution, with gyration radii as low as 15 Å (compactly folded chains) and as large as 40 Å (loosely folded chains).

As shown in Figure 10, for each of the four protonation fractions considered, we find within statistical errors the same rising quasi-linear dependencies of the ensemble- and time-averaged gyration radius ($\langle R_g \rangle$) and end-to-end distance ($\langle D_{ee} \rangle$) on the chain size as in our previous paper. The dependencies for unprotonated and 1/4-protonated chains indicate on average more compact polymer folding and emergent saturation tendency. The similar upward shift of the R_g and D_{ee} profiles with the protonation fraction is a clear indication of the substantial contribution of the supplementary electrostatic repulsion between protonated monomers.

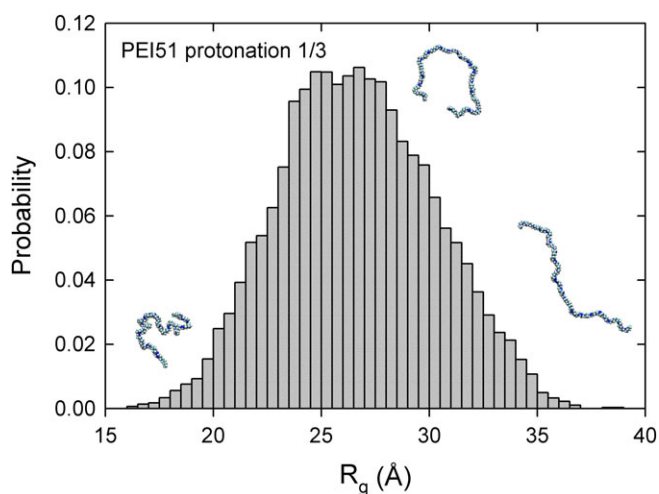


Figure 9. Time- and ensemble-averaged gyration radius distribution for the 1/3-protonated PEI51u3 chain, along with illustrative conformations. [Color figure can be viewed at wileyonlinelibrary.com]

The gyration radius and end-to-end distance averaged over the total data collection time for the unprotonated and 1/2-protonated PEI 51-mer are compared in Table 4 with our previous results and those of Choudhury et al.^[13] for the closest matching chain length (PEI 50-mer). Minding the difference of one monomer between the compared polymers, our present and old results agree within statistical errors, clearly confirming again larger spatial extents, and, implicitly, increased rigidity of our PEI chains as compared to those reported in Ref. 13.

The continuous worm-like chain model^[33] offers an intuitive measure of a polymer's stiffness, namely the persistence length λ . This is, essentially, the length above which thermal fluctuations are able to bend the chain, and it is used to relate the average squared end-to-end distance to the fully extended polymer length L :

$$\langle D_{ee}^2 \rangle = 2\lambda L \left[1 - \frac{\lambda}{L} \left(1 - e^{-\frac{L}{\lambda}} \right) \right], \quad (4)$$

By fitting the time- and ensemble-averaged values of $\langle D_{ee}^2 \rangle$ resulting from our simulations (see Fig. 11) to the above model, we obtained the rough estimates $\lambda \approx 4, 10,$ and 16 \AA for the protonation fractions 0, 1/4, and 1/2, respectively. Although the model fairly describes unprotonated chains, for protonated PEI, the fitting curves can be seen to quite substantially deviate from the simulated data. This finding is readily understood considering that the model is conceived for polymers composed of identical segments, and that only *short-range* (by no means electrostatic) interactions are considered. In particular, the persistence length that we obtained for unprotonated PEI ($4.0 \pm 0.1 \text{ \AA}$) indicates a slightly reduced stiffness as compared to our previous result ($4.8 \pm 0.2 \text{ \AA}$) and it is consistent with the value computed by Lee^[34] for polyethylene oxide ($4.3 \pm 0.3 \text{ \AA}$).

Coordination. We characterize the structuring of the solution about the PEI chains by coordination numbers, taking as references the backbone N and C atoms, specifically, the atom

types NH1, NH2P, CH2, and CH2P. We defined each coordination number as the average number of neighbors within the first coordination shell, and evaluated it from the integral over the first peak of the respective radial distribution function (RDF), by using a rigorous methodology for identifying the peak's limits described in our previous paper.^[20]

Illustrations of RDFs for the backbone atoms with the O water atoms and Cl^- counterions are depicted in Figures 12a and 12b for the unprotonated, 1/4-protonated, and 1/2-protonated 51-mer. As a general remark, protonation gives rise to better defined radial structuring (see comparatively the profiles for NH1 vs. NH2P and CH2 vs. CH2P), with more pronounced major peaks. For NH2P, in particular, the major peak is located at a lower interatomic distance than for NH1 when embedded in protonated chains. This is a natural consequence of the fact that the NH2 (HN2P–NH2P–HN2P) group is positive ($+0.262e$), whereas the NH (NH1–HNH1) group is negative ($-0.428e$). As a result, in the vicinity of protonated amino groups, the water molecules adopt on average orientations with the negatively charged O atoms ($-0.834e$) closer to NH2P than to NH1. For similar reasons, the Cl^- counterions also adopt closer positions to the NH2P atoms.

The O- and Cl^- -coordination numbers, plotted in Figure 13 and Supporting Information Figure S3 as functions of the chain protonation fraction, provide an inclusive image on the

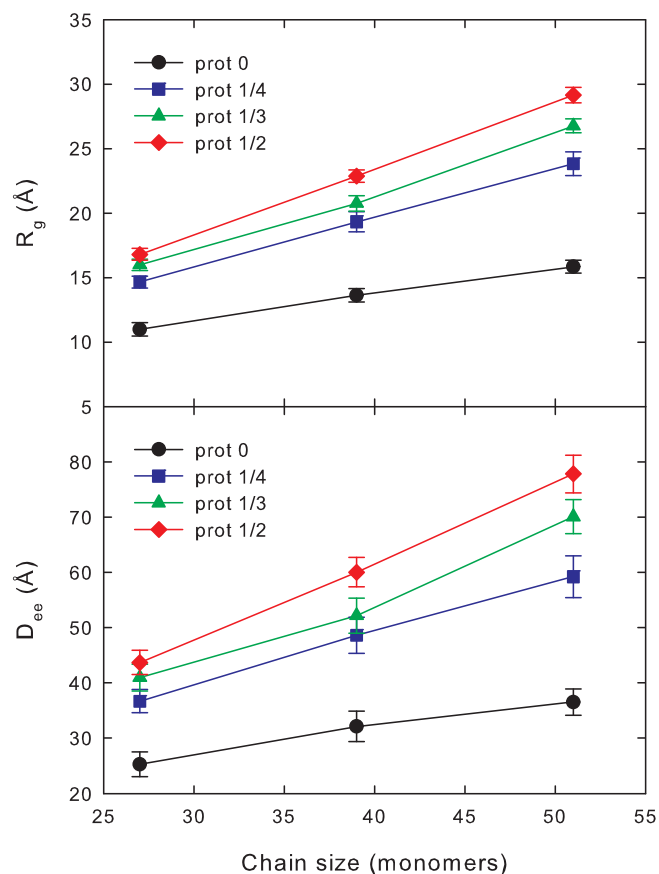


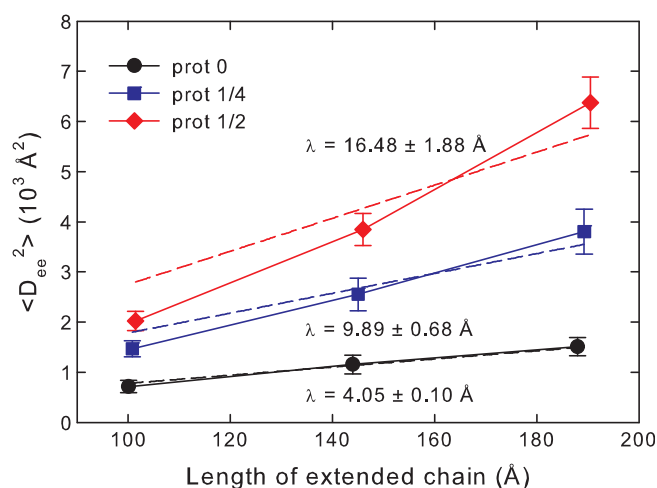
Figure 10. Chain size dependence of the ensemble- and time-averaged gyration radius and end-to-end distance for solvated PEI 27-, 39- and 51-mers. [Color figure can be viewed at wileyonlinelibrary.com]

Table 4. Comparison of the ensemble- and time-averaged radius of gyration and end-to-end distance for the longest PEI chains with our previous results^[20] and those of Choudhury et al.^[13] The total data collection time is indicated.

	Size	Time	Nonprotonated		1/2-protonated	
	-mer	(ns)	R_g	D_{ee}	R_g	D_{ee}
This work	51	400	15.8 ± 0.5	36.5 ± 2.4	29.1 ± 0.6	77.8 ± 3.4
Ref. 20	50	680	16.3 ± 0.5	39.6 ± 2.1	26.4 ± 0.5	70.2 ± 2.7
Ref. 13	50	50	12.3 ± 1.2	32.5 ± 7.7	24.1 ± 2.5	67.7 ± 13.4

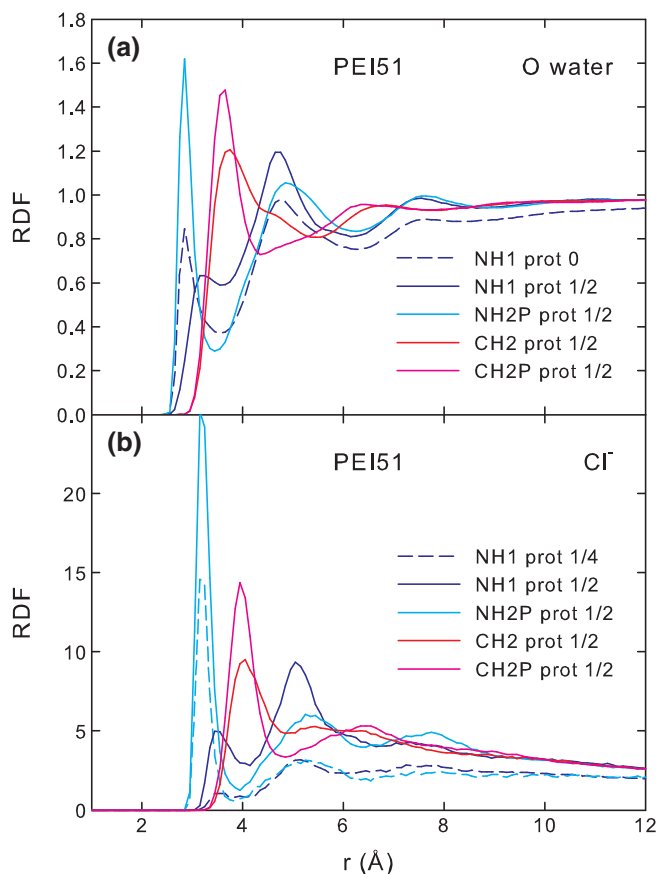
coordination shells about the N and C backbone atoms. As a first remark, the O coordination is invariable with the protonation fraction (except for CH₂), and virtually there is no dependence on the chain length (owing to the identical protonation fractions used for all lengths). Also, the values for the N species are visibly lower than those for the C species, both relative to O and Cl⁻. Given the negatively charged N atoms and the positively charged C atoms, the higher abundance of O and Cl⁻ about the latter is understandable. Using similar reasoning as in the preceding paragraph, the positive net charge also explains the higher O-coordination number for the protonated amino group (~2.5) as compared to the unprotonated one (~2.0).

The particularity that, of all the backbone atom types, only CH₂ displays a notable increase of the O-coordination with the protonation fraction (see Fig. 13) correlates with the existence of a secondary peak in the CH₂-O RDF, partially overlapping the main peak (on the higher r side in Fig. 12a) and making the rigorous identification of the latter's extent difficult. The additional peak actually accounts for a secondary path along which the water O atoms are able to approach CH₂ avoiding the HNH1 atoms of the neighboring amino groups. As already pointed out, the higher the protonation density, the stiffer and more stretched are the PEI chains, thus favoring more extended access regions to the polymer's backbone for the O atoms. Also, noting that the H coordination about CH₂ decreases with increasing protonation fraction creates the overall image in which the water molecules from the first coordination sphere

**Figure 11.** Mean squared end-to-end distances for unprotonated, 1/4- and 1/2-protonated PEI chains as function of their fully extended lengths, along with (dashed) fitting curves for the worm-like chain model, yielding the corresponding persistence lengths λ . [Color figure can be viewed at wileyonlinelibrary.com]

tend to rotate with the O atoms closer and the H atoms further away from the CH₂ atoms.

Contrasting with the relatively insensitive O coordination, and albeit limited to low values by the small Cl⁻ concentrations employed, the Cl⁻-coordination numbers for the protonated types NH₂P and CH₂P are markedly enhanced by protonation (see Supporting Information Fig. S3). This is clearly a geometric effect reflecting the fact that increased density of protonated sites along a folded polymer favors enhanced sharing of the counterion coordination shells, thereby leading to increased coordination numbers. The shift of the CH₂P-Cl⁻ coordinations to higher values relative to the NH₂P-Cl⁻ profiles stems from the genuinely attractive CH₂P-Cl⁻ electrostatic interaction, whereas Cl⁻ experiences attraction only to the entire NH₂ (HN₂P-NH₂P-HN₂P) group. The small but steady shift of the Cl⁻-coordination profiles for the different polymer sizes is

**Figure 12.** Radial distribution functions for a) O water atoms and b) Cl⁻ counterions relative to the N and C backbone atoms of the PEI 51-mer. [Color figure can be viewed at wileyonlinelibrary.com]

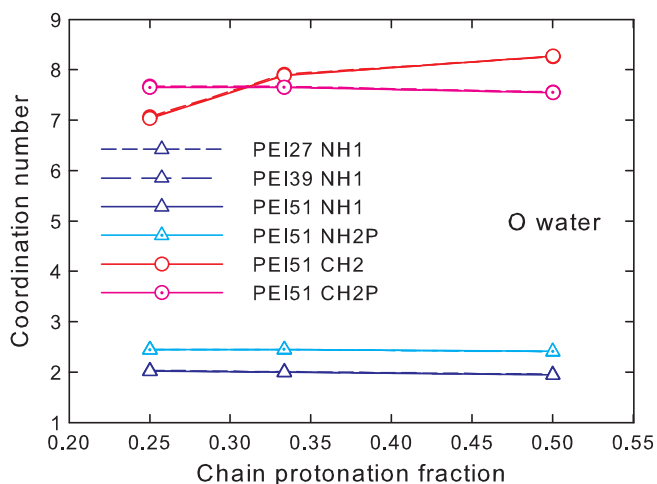


Figure 13. Oxygen-coordination numbers for the N and C backbone atoms as functions of the PEI chain protonation fraction. [Color figure can be viewed at [wileyonlinelibrary.com](#)]

caused by the disparate counterion concentrations resulting from the simulation box volumes which are not proportional to the chain lengths.

Diffusion. To describe the mobility of solvated PEI chains, we evaluated the diffusion coefficient of the polymers based on the commonly used Einstein relation:

$$D = \lim_{t \rightarrow \infty} \frac{1}{6t} \langle \Delta \mathbf{r}_{\text{CM}}(t)^2 \rangle \quad (5)$$

where $\langle \Delta \mathbf{r}_{\text{CM}}(t)^2 \rangle$ is the ensemble-averaged mean squared displacement (MSD) of the chain's center of mass relative to an (initial) reference position.

The time dependencies of the MSD, depicted in Figure 14 for all protonation fractions of the shortest (PEI27) and longest (PEI51) chains, are quasi-linear in the limit of statistical errors, in accordance with the general theory. Nevertheless, the quite ample fluctuations suggest that significantly larger trajectory

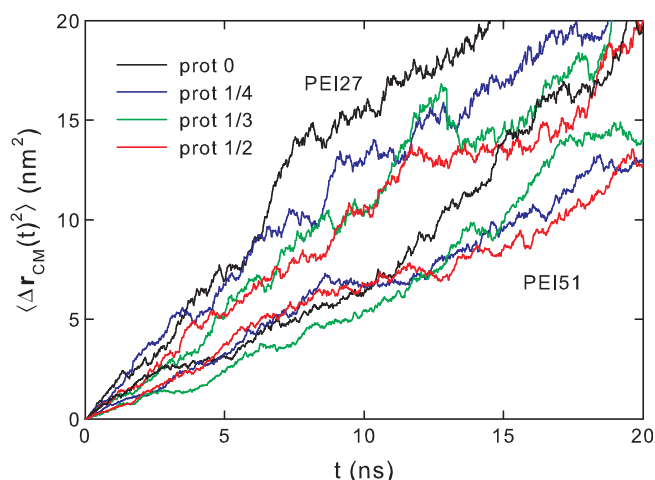


Figure 14. Time dependence of the ensemble-averaged mean square displacement of the PEI center of mass for the PEI 27- and 51-mers. [Color figure can be viewed at [wileyonlinelibrary.com](#)]

ensembles would have been necessary for qualitatively better statistics. The average slopes decrease in groups with increasing PEI chain size, and for a given size, with the protonation fraction. As more expanded and longer polymers naturally feature lower mobility, this behavior is perfectly consistent with the earlier finding that higher protonation brings about additional stiffness, increasing the average spatial extent of the PEI chain.

Overall, the diffusion coefficients evaluated from the ensemble-averaged MSDs decrease both with the protonation fraction and chain size (Fig. 15), for reasons emphasized above. In particular, the deviations from the general trend noted for PEI39 do not reflect genuine phenomenology, but rather can be ascribed to insufficient statistics and underestimated errors. It should also be noted that the error bars roughly follow the magnitude of the diffusion coefficient, with the shortest PEI affected, as expected, by the largest errors.

The resulted diffusion coefficients are perfectly in line with our previous results.^[20] Specifically, the value $1.20 \times 10^{-6} \text{ cm}^2 \text{ s}^{-1}$ that we obtained for the unprotonated PEI51 (molecular weight 2226) exactly matches the fluorescence spectroscopy measurement of Clamme et al.^[35] on branched PEI chains of molecular weight 2500. Moreover, this result also agrees fairly with the experimental value of Hostetler et al.^[36] ($1.34 \times 10^{-6} \text{ cm}^2 \text{ s}^{-1}$) for PEI chains of molecular weight 2140. The overall decay of our diffusion coefficients with increasing chain size is consistent with a similar trend reported by Hostetler et al. for chains of larger molecular weight.

Conclusions

We developed a revised version of our previously published CHARMM FF for unprotonated/protonated PEI chains.^[20] The present FF is solely based on *symmetric* residue types, which is the major difference with regard to our previous model, entailing several improvements. The reduced number of residue and atom types enables a more reliable parameter adjustment and a simplified definition of chains of arbitrary size and protonation pattern. The *enlarged set* of model polymers from which a

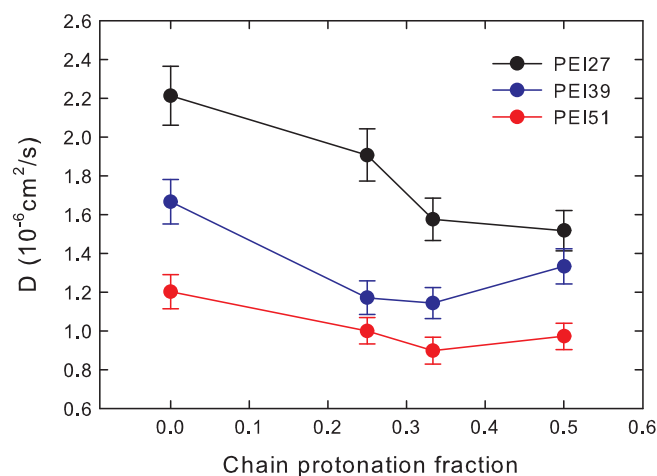


Figure 15. Variation of the diffusion coefficient for PEI 27-, 39-, and 51-mers with the protonation fraction. [Color figure can be viewed at [wileyonlinelibrary.com](#)]

streamlined number of parameters were determined measurably enhances the realism of the FF. Moreover, in contrast with other parametrizations, we optimized the *complete* set of bonded parameters (not only the dihedrals), jointly with the atomic charges, relative to high-quality ab initio calculations.

In broad lines, the present FF is consistent with our previous one,^[20] providing similar MD results. Quite a few of the new bonded parameters (particularly the force constants and equilibrium lengths for bonds) differ by only a few percent from their old values and can be regarded as corrections. Moreover, a highly beneficial trait of the present FF is that it allows for straightforward CG by direct identification of its symmetric residues with individual beads.


As compared to earlier FF parametrizations for PEI, our model basically features increased rigidity resulting in more expanded spatial configurations (increased gyration radius and end-to-end distance). The extensive data collection times that we achieved enabled the in-depth analysis of the chain-length/protonation-fraction dependencies of the various dynamic structural quantities of interest. Remarkably, our simulated diffusion coefficients excellently agree with the available experimental data. Its validated realism makes the developed CHARMM FF model suitable for large-scale atomistic simulations of solvated protonated PEI chains, individually or as part of DNA-PEI polyplexes, which are of current interest to drug-delivery protocols.

Acknowledgments

This work was supported by the Romanian National Authority for Scientific Research and Innovation, CNCS - UEFISCDI (PN-III-P4-ID-PCE-2016-0474).

Keywords: cationic polymers · polyethyleneimine · atomistic force fields · molecular dynamics

How to cite this article: T. A. Beu, A.-E. Ailenei, A. Farcaş, *J. Comput. Chem.* **2018**, 9999, 1–12. DOI: 10.1002/jcc.25637

 Additional Supporting Information may be found in the online version of this article.

- [1] R. Narain, Ed., *Polymers and Nanomaterials for Gene Therapy*, Elsevier, Cambridge, MA, **2016**.
- [2] E. Fleige, M. A. Quadir, R. Haag, *Adv. Drug Deliv. Rev.* **2012**, 64, 866.
- [3] X. Guo, L. Huang, *Acc. Chem. Res.* **2012**, 45, 971.
- [4] M. M. Yallapu, M. Jaggi, S. C. Chauhan, *Drug Discov. Today* **2011**, 16, 457.
- [5] N. Martinho, C. Damge, C. P. Reis, *J. Biomater. Nanobiotechnol.* **2011**, 2, 510.
- [6] E. J. Denning, U. D. Priyakumar, L. Nilsson, A. D. MacKerell, *J. Comput. Chem.* **2011**, 32, 1929.
- [7] K. Hart, N. Foloppe, C. M. Baker, E. J. Denning, L. Nilsson, A. D. MacKerell, *J. Chem. Theory Comput.* **2011**, 8, 348.
- [8] J. Ziebarth, Y. Wang, *Biophys. J.* **2009**, 97, 1971.
- [9] J. Wang, P. Cieplak, P. A. Kollman, *J. Comput. Chem.* **2000**, 25, 1049.
- [10] C. I. Bayly, P. Cieplak, W. D. Cornell, P. A. Kollman, *J. Phys. Chem.* **1993**, 97, 10269.
- [11] J. D. Ziebarth, Y. Wang, *Biomacromolecules* **2010**, 11, 29.
- [12] J. D. Ziebarth, D. R. Kennetz, N. J. Walker, Y. Wang, *J. Phys. Chem. B* **2017**, 121, 1941.
- [13] C. K. Choudhury, S. Roy, *Soft Matter* **2013**, 9, 2269.
- [14] D. A. Kondinskaia, A. Y. Kostritskii, A. M. Nesterenko, A. Y. Antipina, A. A. Gurtovenko, *J. Phys. Chem. B* **2016**, 120, 6546.
- [15] C. Sun, T. Tang, H. Uludağ, J. E. Cuervo, *Biophys. J.* **2011**, 100, 2754.
- [16] A. D. MacKerell, N. Banavali, N. Foloppe, *Biopolymers* **2001**, 56, 257.
- [17] Z. Wei, E. Luijten, *J. Chem. Phys.* **2015**, 143, 243146.
- [18] K. Vanommeslaeghe, E. Hatcher, C. Acharya, S. Kundu, S. Zhong, J. Shim, E. Darian, O. Guvench, P. Lopes, I. Vorobyov, A. D. MacKerell, Jr., *J. Comput. Chem.* **2010**, 31, 671.
- [19] C. G. Mayne, J. Saam, K. Schulten, E. Tajkhorshid, J. C. Gumbart, *J. Comput. Chem.* **2013**, 34, 2757.
- [20] T. A. Beu, A. Farcaş, *J. Comput. Chem.* **2017**, 38, 2335.
- [21] A. D. MacKerell Jr., D. Bashford, M. Bellott, R. L. Dunbrack Jr., J. D. Evanseck, M. J. Field, S. Fischer, J. Gao, H. Guo, S. Ha, D. Joseph-McCarthy, L. Kuchnir, K. Kuczera, F. T. K. Lau, C. Mattos, S. Michnick, T. Ngo, D. T. Nguyen, B. Prodhom, W. E. Reiher, B. Roux, M. Schlenkrich, J. C. Smith, R. Stote, J. Straub, M. Watanabe, J. Wiórkiewicz-Kuczera, D. Yin, M. Karplus, *J. Phys. Chem. B* **1998**, 102, 3586.
- [22] C. G. Mayne, Rapid parameterization of small molecules using the force field toolkit, <http://www.ks.uiuc.edu/Training/Tutorials/science/ffTK/fftk-tutorial.pdf> (accessed September 2015).
- [23] W. Humphrey, A. Dalke, K. Schulten, *J. Molec. Graphics* **1996**, 14, 33.
- [24] M. J. Frisch, G. W. Trucks, H. B. Schlegel, G. E. Scuseria, M. A. Robb, J. R. Cheeseman, G. Scalmani, V. Barone, G. A. Petersson, H. Nakatsuji, X. Li, M. Caricato, A. Marenich, J. Bloino, B. G. Janesko, R. Gomperts, B. Mennucci, H. P. Hratchian, J. V. Ortiz, A. F. Izmaylov, J. L. Sonnenberg, D. Williams-Young, F. Ding, F. Lipparini, F. Egidi, J. Goings, B. Peng, A. Petrone, T. Henderson, D. Ranasinghe, V. G. Zakrzewski, J. Gao, N. Rega, G. Zheng, W. Liang, M. Hada, M. Ehara, K. Toyota, R. Fukuda, J. Hasegawa, M. Ishida, T. Nakajima, Y. Honda, O. Kitao, H. Nakai, T. Vreven, K. Throssell, J. A. Montgomery, Jr., J. E. Peralta, F. Ogliaro, M. Bearpark, J. J. Heyd, E. Brothers, K. N. Kudin, V. N. Staroverov, T. Keith, R. Kobayashi, J. Normand, K. Raghavachari, A. Rendell, J. C. Burant, S. S. Iyengar, J. Tomasi, M. Cossi, J. M. Millam, M. Klene, C. Adamo, R. Cammi, J. W. Ochterski, R. L. Martin, K. Morokuma, O. Farkas, J. B. Foresman, D. J. Fox, *Gaussian 09 Revision A.01*, Gaussian Inc., Wallingford, CT, **2009**.
- [25] MacKerell Lab Homepage, CHARMM force field files, http://mackerell.umaryland.edu/charmm_ff.shtml
- [26] J. C. Phillips, R. Braun, W. Wang, J. Gumbart, E. Tajkhorshid, E. Villa, C. Chipot, R. D. Skeel, L. Kale, K. Schulten, *J. Comput. Chem.* **2005**, 26, 1781.
- [27] J.-P. Ryckaert, G. Ciccotti, H. J. Berendsen, *J. Comput. Phys.* **1977**, 23, 327.
- [28] W. L. Jorgensen, J. Chandrasekhar, J. D. Madura, R. W. Impey, M. L. Klein, *J. Chem. Phys.* **1983**, 79, 926.
- [29] U. Essmann, L. Perera, M. L. Berkowitz, T. Darden, H. Lee, L. G. Pedersen, *J. Chem. Phys.* **1995**, 103, 8577.
- [30] G. J. Martyna, D. J. Tobias, M. L. Klein, *J. Chem. Phys.* **1994**, 101, 4177.
- [31] S. E. Feller, Y. Zhang, R. W. Pastor, B. R. Brooks, *J. Chem. Phys.* **1995**, 103, 4613.
- [32] I. Perevyazko, A. S. Gubarev, L. Tauhardt, A. Dobrodumov, G. M. Pavlov, U. S. Schubert, *Polym. Chem.* **2017**, 8, 7169.
- [33] O. Kratky, G. Porod, *Recl. Trav. Chim. Pays. Bas.* **1949**, 68, 1106.
- [34] H. Lee, R. M. Venable, A. D. MacKerell, Jr., R. W. Pastor, *Biophys. J.* **2008**, 95, 1590.
- [35] J. P. Clamme, J. Azoulay, Y. Mely, *Biophys. J.* **2003**, 84, 1960.
- [36] R. E. Hostetler, J. W. Swanson, *Aust. J. Polit. Sci.* **1974**, 12, 29.

Received: 1 August 2018

Revised: 14 September 2018

Accepted: 14 September 2018